PHOTONICS Research

Enhancement of phase conjugation degenerate four-wave mixing using a Bessel beam

Qian Zhang,[1,†] Xuemei Cheng,[1,*,†] Haowei Chen,[1,3] Bo He,[1] Zhaoyu Ren,[1] Ying Zhang,[2] and Jintao Bai[1]

[1]State Key Laboratory Incubation Base of Photoelectric Technology and Functional Materials, National Photoelectric Technology and Functional Materials and Application of Science and Technology International Cooperation Center, Institute of Photonics & Photon-Technology, Northwest University, Xi'an 710069, China
[2]School of Science, Engineering University of PAP, Xi'an 710086, China
[3]e-mail: chenhaowei2005@126.com
*Corresponding author: xmcheng@nwu.edu.cn

Received 26 October 2017; revised 7 December 2017; accepted 22 December 2017; posted 3 January 2018 (Doc. ID 310019); published 12 February 2018

We report on the enhancement of phase conjugation degenerate four-wave mixing (DFWM) in hot atomic Rb vapor by using a Bessel beam as the probe beam. The Bessel beam was generated using cross-phase modulation based on the thermal nonlinear optical effect. Our results demonstrated that the DFWM signal generated by the Bessel beam is about twice as large as that generated by the Gaussian beam, which can be attributed to the extended depth and tight focusing features of the Bessel beam. We also found that a DFWM signal with reasonable intensity can be detected even when the Bessel beam encounters an obstruction on its way, thanks to the self-healing property of the Bessel beam. This work not only indicates that DFWM using a Bessel beam would be of great potential in the fields of high-fidelity communication, adaptive optics, and so on, but also suggests that a Bessel beam would be of significance to enhance the nonlinear process, especially in thick and scattering media.

OCIS codes: (190.4380) Nonlinear optics, four-wave mixing; (350.6830) Thermal lensing; (060.5060) Phase modulation.

https://doi.org/10.1364/PRJ.6.000162

1. INTRODUCTION

Bessel beams are radiations of which the amplitudes can be described by Bessel functions, which are sets of solutions to the Helmholtz equation in free space [1]. As they exhibit the propagation-invariant feature (non-diffraction) [2–5], people can achieve an extended depth of field with a small focal spot using Bessel beams. Moreover, they have the ability to reestablish their transverse intensity profiles after passing through an obstacle (self-healing, self-reconstructing). For those attractive properties, Bessel beams have been applied in numerous areas, such as atom optics [6,7], optical micromanipulation [2], microscopy [8–10], and optical tweezers [11]. Bessel beams are also of particular significance in nonlinear optics [12–14]. On one hand, nonlinear optical processes can be enhanced (especially in thick and complex media), thanks to the "non-diffraction" and "self-reconstructing" properties of the Bessel beam. On the other hand, more information of the nonlinear medium can be retrieved because of the unique phase-matching characteristics across the focal region.

Four-wave mixing (FWM) is a kind of third-order nonlinear process in which three beams interact with the nonlinear medium and a fourth beam (FWM signal) is generated when the phase-matching condition is satisfied. FWM has a variety of applications, such as squeezed states of light [15], wavelength conversion [16], isotope selective analysis and determination [17,18], and image reconstruction [19,20]. In particular, degenerate FWM (DFWM) is a superb method to generate a phase-conjugate beam, in which a probe beam intersects two counter-propagating pump beams, and the DFWM signal is generated in the opposite direction of the probe beam. Because the DFWM signal is the phase-conjugate beam of the input probe beam, it can be used to eliminate the distortion as the probe beam passes through an inhomogeneous phase-distorting medium [21,22]. So far, DFWM has been widely used in adaptive optics, laser communication, and so on. However, the DFWM signal decreases or even disappears due to phase-mismatching and loss of energy in a strongly scattering thick medium, limiting its application in harsh environments.

In this work, we use a Bessel beam as the probe beam and study the enhancement of DFWM in hot atomic Rb vapor. The Bessel beam is generated by focusing the hollow beam generated using cross-phase modulation based on the thermal nonlinear optical effect [23]. Compared with commonly used hollow beam generation methods (including axicon lenses [24]

and spatial light modulators [25]), the method employed in this work has the advantages of tunable size and no limitation of the input power. With the help of such a method, we were able to vary the size of the hollow beam to get a Bessel beam with appropriate size and desirable non-diffraction length. This method also allowed us to set the power of the probe beam to be several megawatts (mW) and to optimize the DFWM generation. We compared the performance of the Bessel beam with a Gaussian beam and found that the Bessel beam can greatly enhance the DFWM process, particularly when an obstruction is set on the path of the input probe beam. This work suggests that DFWM using a Bessel beam is of significant potential in the fields of high-fidelity communication, adaptive optics, and so on.

2. METHOD

Figure 1 is the layout of the experimental setup we used. The light source is a continuous wave wavelength tunable Ti:sapphire laser (Spectra-Physics, Matisse TR, 750–990 nm), with beam diameter of 1.4 mm. A built-in wavelength meter (Highfinesse, WS/6 200) is used to monitor the laser wavelength. The setup mainly includes two parts: DFWM and hollow beam generation.

DFWM. The laser output was first split into two beams by the combination of a half-wave plate (HWP) and a polarization beam splitter (PBS1). The transmission from PBS1 provides the backward pump field $\boldsymbol{E}_{\mathrm{b}}(\omega, \boldsymbol{k}_{\mathrm{b}})$, and the reflection beam is further split into two beams by PBS2. The reflection of PBS2 is employed as the forward pump field $\boldsymbol{E}_{\mathrm{f}}(\omega, \boldsymbol{k}_{\mathrm{f}})$, and the transmission is used to generate the hollow beam. The generated hollow beam serves as the probe field $\boldsymbol{E}_{\mathrm{p}}(\omega, \boldsymbol{k}_{\mathrm{p}})$. The experiment is conducted in a two-level atomic system, composed of energy levels $|a\rangle$ and $|b\rangle$, in which $|a\rangle$ and $|b\rangle$ stand for $|5S_{1/2}, F = 3\rangle$ of ^{85}Rb and $|5P_{3/2}, F = 2, 3, 4\rangle$ of ^{85}Rb [26], respectively. The phase-matching configuration of the DFWM process is shown in the right bottom part of Fig. 1, the beam $\boldsymbol{E}_{\mathrm{f}}$ and the beam $\boldsymbol{E}_{\mathrm{b}}$ are counter-propagating with each other, and $\boldsymbol{E}_{\mathrm{p}}$ intersects with the forward pump field $\boldsymbol{E}_{\mathrm{f}}$ at a small angle (less than 0.01 rad). With the phase-matching condition ($\boldsymbol{k}_{\mathrm{f}} + \boldsymbol{k}_{\mathrm{b}} = \boldsymbol{k}_{\mathrm{p}} + \boldsymbol{k}_{\mathrm{s}}$), the DFWM signal $\boldsymbol{E}_{\mathrm{s}}(\omega, \boldsymbol{k}_{\mathrm{s}})$ is generated in the opposite direction of $\boldsymbol{E}_{\mathrm{p}}$, which is detected by silicon detector (Zolix, Dsi200, 10 mm × 10 mm, 200–1100 nm) or imaged by a CMOS camera (Thorlabs, DD1240M, 1280 × 1240, 6.78 mm × 5.43 mm). The sample is atomic Rb vapor contained in a 10 cm long vacuumed cell (5×10^{-5} Pa) without buffer gas in it. The cell is heated by a heater band with an electrical temperature controller.

Hollow beam generation. The transmission through PBS2 is split into two beams by PBS3, the reflection is denoted as weak beam $\boldsymbol{E}_{\mathrm{w}}$, and the transmission is denoted as intense beam $\boldsymbol{E}_{\mathrm{in}}$. The beam $\boldsymbol{E}_{\mathrm{in}}$ passes through an HWP, an $f = 200$ mm Lens1, PBS4, and then into the cuvette with ethanol. The beam $\boldsymbol{E}_{\mathrm{w}}$ is guided into the cuvette with ethanol in the opposite direction of $\boldsymbol{E}_{\mathrm{in}}$. The output $\boldsymbol{E}_{\mathrm{w}}$ from the cuvette with ethanol is reflected by PBS4, collimated by a telescope system (Lens2 and Lens3), and then employed as the probe field $\boldsymbol{E}_{\mathrm{p}}(\omega, \boldsymbol{k}_{\mathrm{p}})$. The output $\boldsymbol{E}_{\mathrm{w}}$ from the cuvette with ethanol can be switched between Gaussian beam and hollow beam by setting the beam $\boldsymbol{E}_{\mathrm{in}}$ off or on [23]. By focusing the hollow beam (Lens5), we can obtain a Bessel beam in the focusing range [27].

In the experiment of studying the influence of obstruction on DFWM, we put a thin quartz plate (0.17 mm thick) in the transmission paths of probe beam $\boldsymbol{E}_{\mathrm{p}}$ and the forward pump beam $\boldsymbol{E}_{\mathrm{f}}$ and then only dropped the black printing ink with the diameter of 1 mm or so in the quartz plate in the transmission path of probe beam $\boldsymbol{E}_{\mathrm{p}}$, denoted as obstruction (Obs) in Fig. 1.

DFWM is a third-order nonlinear optical effect. The induced third-order atomic polarization $P^{(3)}$ is derived from the perturbation theory as [18]

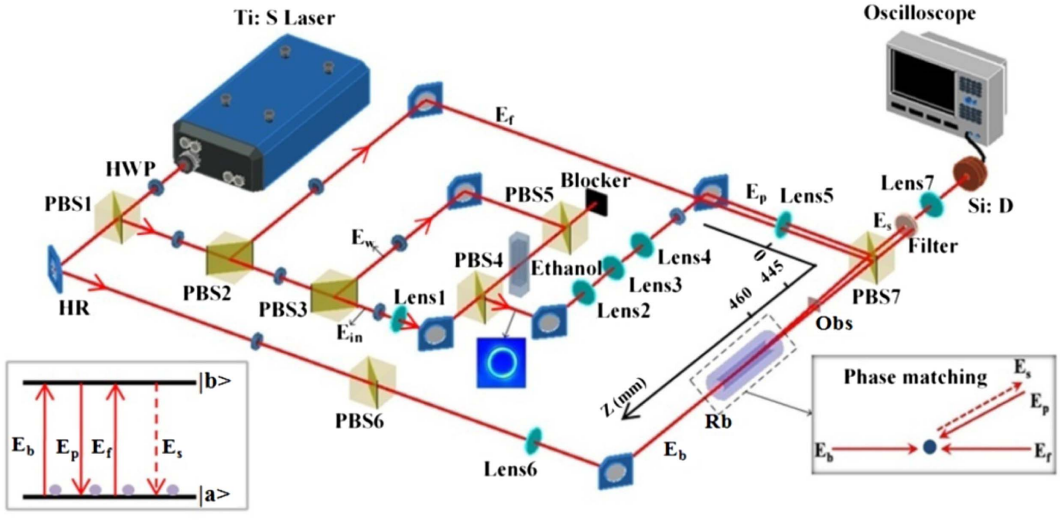

Fig. 1. Scheme of the experimental setup. The insert located at the bottom left is the energy-level diagram we employed in which $|a\rangle$ and $|b\rangle$ stand for $|5S_{1/2}, F = 3\rangle$ of ^{85}Rb and $|5P_{3/2}, F = 2, 3, 4\rangle$ of ^{85}Rb, respectively. The insert at the bottom right is the phase-matching configuration of the DFWM process. The coordinate z stands for the propagating direction of the probe beam originated from Lens5. The obstruction is inserted at $z = 445$ mm, and the Rb cell is set with its right side at $z = 460$ mm. Ti:S laser, Ti:sapphire laser; HWP, half-wave plate; HR, highly reflective mirror; PBS, polarization beam splitter; Obs, obstruction; Si:D, silicon detector. Ethanol is contained in a cuvette.

$$P^{(3)} = 4N|\mu_{ba}|^4\hbar^{-3}E_f E_b E_p^* \frac{T_1}{T_2} \times \frac{1}{(\Delta + i/T_2)[(\Delta + i/T_2)(-\Delta + i/T_2) - \Omega^2]}, \quad (1)$$

where μ_{ba} is the electric dipole moment between energy level $|5S_{1/2}, F = 3\rangle$ and $|5P_{3/2}, F = 2, 3, 4\rangle$ of ^{85}Rb, Δ is the frequency detuning, N is the atomic number density, Ω is the Rabi frequency, and T_1 and T_2 are the lifetimes of the upper level ($|b\rangle$) and the dipole dephasing time, respectively. The DFWM signal intensity is $I_F \propto |P^{(3)}|^2$.

The hollow beam generation can be theoretically explained by the thermal nonlinear optical effect. When an intense laser beam passes through the cuvette with ethanol, the refractive index n of the ethanol becomes laser intensity dependent,

$$n = n_0 + n_2 I_{in}, \quad (2)$$

where n_0 is the linear refractive index, I_{in} is the intensity of the intense beam, and n_2 is the nonlinear refractive coefficient caused by thermal nonlinear effect, expressed as [23]

$$n_2 = \left(\frac{dn}{dT}\right)\frac{\alpha\omega_p^2}{\kappa}, \quad (3)$$

where dn/dT describes the temperature dependence of the refractive index of a given nonlinear medium, α is the absorption coefficient, ω_p is the beam radius, and κ is the thermal conductivity. The distribution of the refractive index applies for any beam that passes through the ethanol at the same area with the intense beam; therefore, an additional lateral phase shift $\Delta\varphi(\rho)$ on the exit plane of the cuvette with ethanol would be generated,

$$\Delta\varphi(\rho) = k_0 \int_0^l n_2 I_{in}(\rho, z)dz = k_0 \int_0^l n_2 I_{in0} \frac{\omega_{i0}^2}{\omega_{inp}^2(z)} \exp\left[\frac{-2\rho^2}{\omega_{inp}^2(z)}\right]dz, \quad (4)$$

in which I_{in0} is the incident central intensity of the intense beam, k_0 is the wave vector, ω_{in0} is the waist radius of the intense beam, $\omega_{inp}(z)$ is the beam radius of the intense beam, ρ is the radial coordinate, and l is the length of the cuvette with ethanol. Getting out of the cuvette with ethanol, the weak beam carrying the nonlinear phase shift will propagate in free space. The far-field distribution pattern can be simulated based on the integral formula of Fresnel–Kirchhoff diffraction,

$$I_w = \left|\frac{1}{i\lambda D}\right|^2 \left| \int_0^\infty \int_0^{2\pi} E_w(0, l) \exp(-ik\rho\theta \cos\phi) \times \exp\left\{-i\left[\frac{k\rho^2}{2R(l)} + \Delta\varphi(\rho)\right]\right\} r dr d\phi \right|^2, \quad (5)$$

in which D is the distance, $R(l)$ is the wavefront curvature radius of the weak beam at the exit side of the cuvette with ethanol, and θ and ϕ are the far-field diffraction angle and the angular coordinate of the exit surface, respectively. As the nonlinear refractive coefficient caused by thermal nonlinear effects n_2 of ethanol is negative (we measured it to be -2.19×10^{-8} cm^2/W with a Z-scan), the ethanol radiated by the intense $\boldsymbol{E}_{in}$ beam takes the defocusing effect on the weak $\boldsymbol{E}_w$ beam. The beam $\boldsymbol{E}_w$ is thus converted into a hollow beam.

3. RESULTS AND DISCUSSION

We first compared the performance of the Bessel beam and the Gaussian beam in a homogenous environment. We set the power of $\boldsymbol{E}_{in}$ as 100 mW and obtained the hollow beam $\boldsymbol{E}_p$ as shown in Fig. 1. The Bessel beam can be obtained in the focusing range of the hollow beam. The Bessel beam generation using such a method based on the cross-phase modulation based on the thermal nonlinear effect has been well characterized in our recent published paper [23]. The probe beam can be switched between a Gaussian and a hollow beam simply by blocking the intense beam $\boldsymbol{E}_{in}$ or not. Then we took either the Gaussian or hollow beam as the probe beam and detected the DFWM spectra and the signal images. The power of $\boldsymbol{E}_b$, $\boldsymbol{E}_f$, and $\boldsymbol{E}_p$ was set at 5, 20, and 20 mW, respectively.

The DFWM spectra were obtained by scanning the laser wavelength around the D2 line of Rb atoms and plotting the integrated intensity of the DFWM signals with respect to the laser frequency detuning, as shown in Fig. 2(a), in which the DFWM power was obtained by integrating the DFWM signal over the entire area of the silicon detector. The curve with higher intensity is generated with a hollow beam as the probe beam, and the one with lower intensity is generated with a Gaussian beam as the probe beam. It is seen that every curve includes four DFWM signal peaks corresponding to the four transitions of Rb D2 lines (a: ^{87}Rb$|5S_{1/2}, F = 1\rangle \rightarrow |5P_{3/2}\rangle$ at 780.2289 nm; b: ^{85}Rb$|5S_{1/2}, F = 2\rangle \rightarrow |5P_{3/2}\rangle$ at 780.2322 nm; c: ^{85}Rb$|5S_{1/2}, F = 3\rangle \rightarrow |5P_{3/2}\rangle$ at 780.2424 nm; d: ^{87}Rb$|5S_{1/2}, F = 2\rangle \rightarrow |5P_{3/2}\rangle$ at 780.2459 nm) [28]. The peak splitting in the spectra is due to the Stark effect, which was studied in detail previously [17].

We then fixed the wavelength at 780.2424 nm (^{85}Rb$|5S_{1/2}, F = 3\rangle \rightarrow |5P_{3/2}\rangle$) and obtained the images of DFWM signal by CMOS. Typical images of the DFWM signal with the hollow and Gaussian beams as the probe beam are shown in Fig. 2(b). A hollow signal is generated with a hollow input probe beam, which is to be expected because the DFWM is the phase-conjugate beam of the incident probe beam.

The enhancement of the power of DFWM signal with the hollow beam as the probe beam can be attributed to the non-diffraction property of the Bessel beam. The Bessel beam

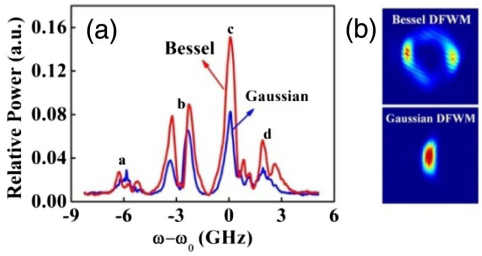

Fig. 2. Enhancement of DFWM signal with hollow input probe beam compared with Gaussian input. (a) Spectra of DFWM signal with hollow and Gaussian beams as the probe beam; (b) DFWM signal images with hollow beam (upper) and Gaussian beam (bottom) at the wavelength of 780.2424 nm, resonant to the transition $|5S_{1/2}, F = 3\rangle \rightarrow |5P_{3/2}\rangle$ of ^{85}Rb. The laser powers of $\boldsymbol{E}_b$, $\boldsymbol{E}_f$, and $\boldsymbol{E}_p$ were set at 5, 20, and 20 mW, respectively, and the temperature of the Rb cell was set at 40°C.

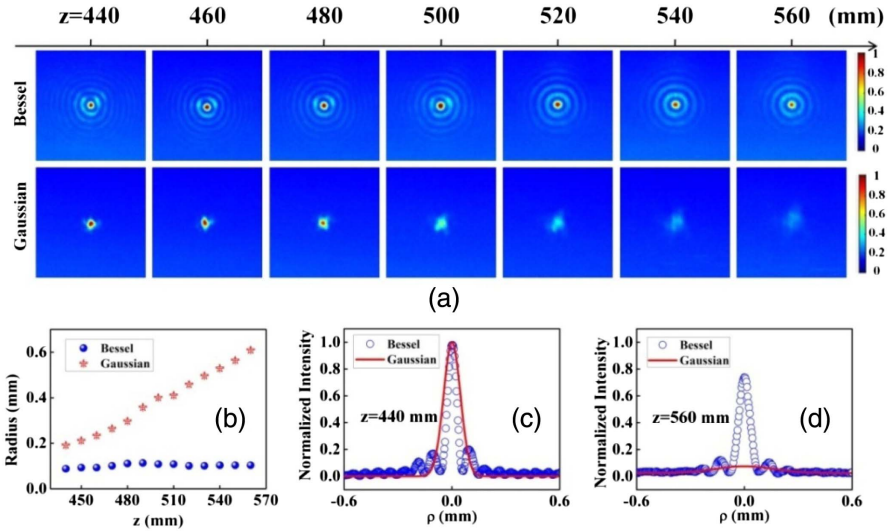

Fig. 3. Comparison of the light propagation properties between Gaussian and Bessel beams. (a) Images of Bessel beam (top row) and Gaussian beam (bottom row) at various positions along the propagation coordinate z in the focusing range. (b) The radius of the central spot of the Bessel beam and the Gaussian beam at various positions along the propagation coordinate z in the focusing range; (c) and (d) show the lateral intensity distribution of the Bessel beam and the Gaussian beam at $z = 440$ mm and $z = 560$ mm, respectively. The power of probe beam $\boldsymbol{E}_{\mathrm{p}}$ was fixed at 1 mW, the laser wavelength was kept at 780.2424 nm, and the temperature of the Rb cell was set at 40°C.

is generated in the focusing range of the hollow laser beam, so we compared the propagation property of the probe Bessel beam with the probe Gaussian beam by taking their intensity distributions at various positions in the focusing region. We took the transmitting direction of the probe beam as the positive direction with the coordinate origin at Lens5 ($f = 500$ mm). The power of probe beam $\boldsymbol{E}_{\mathrm{p}}$ was fixed at 1 mW, and the laser wavelength was fixed as 780.2424 nm (resonant to the transition $|5S_{1/2}, F = 3\rangle \rightarrow |5P_{3/2}\rangle$ of ^{85}Rb). The beam profiles at various positions were detected by CMOS. In Fig. 3(a), the upper row shows the images of the Bessel beam and the bottom row shows the images of the Gaussian beam. We collected the information of the beam size (central spot) from the images and then plotted the data in Figs. 3(b)–3(d). It is seen from Fig. 3(b) that the central spot size of the Bessel beam remains invariable, while with the Gaussian beam divergence occurs in the propagation direction. The radius of Gaussian beam increases from 0.2 to 0.6 mm after propagating 120 mm. In contrast, the radius of the bright central spot of the Bessel beam almost remains constant as 0.1 mm. Figs. 3(c) and 3(d) show the lateral intensity profiles of the Bessel beam and the Gaussian beam at $z = 440$ mm and $z = 560$ mm, respectively. It is seen that the intensity of the Gaussian beam decreases by 95% at $z = 560$ mm. In contrast, the intensity of the Bessel beam decreases only by 20% or so. From the description above, we can see that the Bessel beam has an extended depth of field and tight focusing features compared with the Gaussian beam, which results in a longer phase-matching distance and effectively enhances the DFWM signal.

We further considered the case in which the probe beam encountered an obstruction on its way to the Rb sample. We inserted a SiO_2 plate (0.17 mm thick) with a drop of black printing ink (diameter of 1 mm or so) on the path of probe beam $\boldsymbol{E}_{\mathrm{p}}$ at $z = 445$ mm (as shown in Fig. 1). The powers of $\boldsymbol{E}_{\mathrm{b}}$, $\boldsymbol{E}_{\mathrm{f}}$, and $\boldsymbol{E}_{\mathrm{p}}$ were still kept as 5, 20, and 20 mW, respectively. The laser wavelength was scanned around the D2 line of the Rb atom. The integrated intensity of the DFWM signals with respect to the laser frequency detuning is shown in Fig. 4(a). It is obvious that no signal was obtained with the Gaussian beam as the probe beam. In contrast, a signal with reasonable intensity was detected with the Bessel beam as the probe beam. Moreover, the signal image shows that the DFWM was still a typical hollow beam [Fig. 4(b)], indicating that the phase-conjugate DFWM signal can efficiently avoid the influence of the obstruction.

The superb performance of the Bessel beam in DFWM when it encounters an obstruction on its way to the Rb sample can be attributed to the self-healing ability of the probe Bessel beam, as shown in Fig. 5, when we insert a SiO_2 plate (0.17 mm) with a drop of black printing ink (diameter of

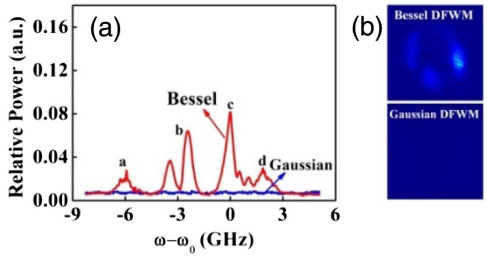

Fig. 4. Enhancement of DFWM signal with hollow input probe beam compared with Gaussian input when the probe beam encounters an obstruction on its propagation way to the Rb sample. (a) Spectra of DFWM signal with hollow and Gaussian beams as the probe beam; (b) DFWM signal images with hollow beam (upper) and Gaussian beam (bottom) at the wavelength of 780.2424 nm, resonant to the transition $|5S_{1/2}, F = 3\rangle \rightarrow |5P_{3/2}\rangle$ of ^{85}Rb. The laser powers of $\boldsymbol{E}_{\mathrm{b}}$, $\boldsymbol{E}_{\mathrm{f}}$, and $\boldsymbol{E}_{\mathrm{p}}$ were set at 5, 20, and 20 mW, respectively, and the temperature of the Rb cell was set at 40°C.

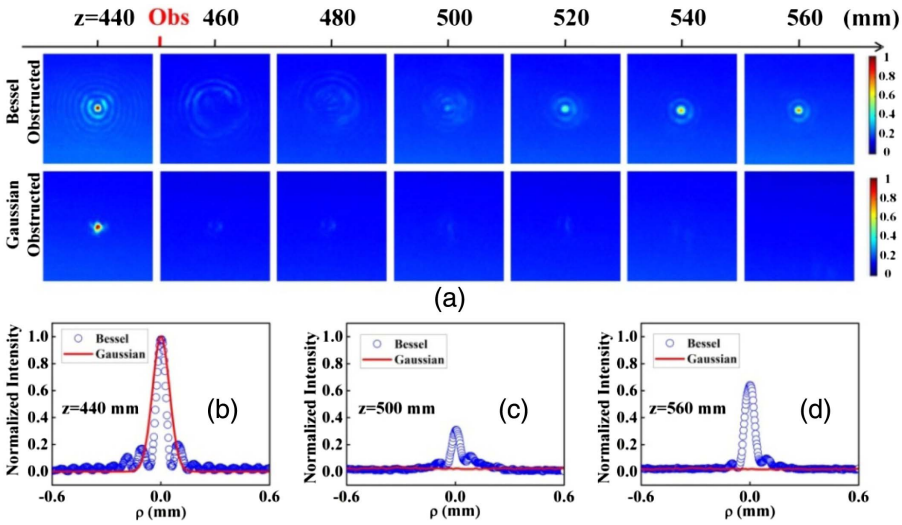

Fig. 5. Self-reconstruction of the Bessel beam and the Gaussian beam. (a) Images of the Bessel beam (upper row) and the Gaussian beam (bottom row) at various positions along the propagation coordinate z when the Gaussian beam and the Bessel beam pass through obstruction; (b)–(d) show the lateral intensity distribution of the Bessel beam and the Gaussian beam at $z = 440$ mm, $z = 500$ mm, and $z = 560$ mm. The power of probe beam $\boldsymbol{E}_{\mathrm{p}}$ was fixed at 1 mW, the laser wavelength was kept at 780.2424 nm, the temperature of the Rb cell was set at 40°C, and the obstruction was set at $z = 445$ mm.

1 mm or so) at $z = 445$ mm. The power of probe beam $\boldsymbol{E}_{\mathrm{p}}$ was fixed at 1 mW, and the laser wavelength was fixed at 780.2424 nm (resonant to the transition $|5S_{1/2}, F = 3\rangle \rightarrow |5P_{3/2}\rangle$ of ^{85}Rb). The beam profiles of the Bessel beam (upper row) and the Gaussian beam (bottom row) at various propagating distances were detected and shown in Fig. 5(a). It is observed that the central bright spot of the Bessel beam is totally blocked by the obstruction at the beginning, and then it recovered as it propagated along the z direction. Figures 5(b)–5(d) show the lateral intensity profiles of the Bessel beam and the Gaussian beam at $z = 440$ mm, $z = 500$ mm, and $z = 560$ mm, respectively. Although the central bright spot of the Bessel beam was totally blocked by the obstruction at the beginning, it recovers itself gradually during propagation. As seen from Figs. 5(c) and 5(d), it recovers by about 30% at $z = 500$ mm and about 70% at $z = 560$ mm, which is lower than the unobstructed case by only 10% [Fig. 3(d)]. The recovered Bessel beam can interact with the Rb atoms together with the two pump beams and generate the DFWM signal. In contrast, the Gaussian beam cannot recover due to the serious divergence and the loss of energy, and no DFWM signal was generated as a consequence.

4. CONCLUSION

In this work, we used a Bessel beam to enhance the DFWM process in hot atomic Rb vapor. The Bessel beam was generated using cross-phase modulation based on thermal nonlinear optical effect. We took either the Bessel beam or the Gaussian beam as the probe beam and compared the DFWM signal under the two cases. The results show that the DFWM signal generated by the Bessel beam is about twice as large as that generated by the Gaussian beam, thanks to the extended depth of field and tight focusing properties of the Bessel beam. Moreover, thanks to self-healing properties of the Bessel beam, a DFWM signal can be detected with the Bessel beam when it encounters an obstruction. In contrast, no DFWM signal was detected using the Gaussian beam as the probe beam. This work suggests that DFWM using a Bessel beam would be of great potential in the fields of high-fidelity communication, adaptive optics, and so on. It would also shed a light on those areas where the nonlinear processes are needed enhancing in some thick media and harsh environments.

Funding. National Natural Science Foundation of China (NSFC) (61475125); Natural Science Foundation of Shaanxi Province (2017JQ6066); Education Department of Shaanxi Province (16JK1776); Northwest University Doctorate Dissertation of Excellence Funds (YYB17006).

†The authors contributed equally to this work.

REFERENCES

1. J. Durnin, J. J. Miceli, and J. H. Eberly, "Comment on diffraction-free beams," Phys. Rev. Lett. **58**, 1499–1501 (1987).
2. F. O. Fahrbach, P. Simon, and A. Rohrbach, "Microscopy with self-reconstructing beams," Nat. Photonics **4**, 780–785 (2010).
3. V. Garcéschávez, D. Mcgloin, H. Melville, W. Sibbett, and K. Dholakia, "Simultaneous micromanipulation in multiple planes using a self-reconstructing light beam," Nature **419**, 145–147 (2002).
4. K. Szulzycki, V. Savaryn, and I. Grulkowski, "Generation of dynamic Bessel beams and dynamic bottle beams using acousto-optic effect," Opt. Express **24**, 23977–23991 (2016).
5. L. Thibon, L. E. Lorenzo, M. Piché, and Y. D. Koninck, "Resolution enhancement in confocal microscopy using Bessel–Gauss beams," Opt. Express **25**, 2162–2176 (2017).
6. S. Schmid, G. Thalhammer, K. Winkler, F. Lang, and J. H. Denschlag, "Long distance transport of ultracold atoms using a 1D optical lattice," New J. Phys. **8**, 159 (2006).
7. J. Arlt and K. Dholakia, "Generation of high-order Bessel beams by use of an axicon," Opt. Commun. **177**, 297–301 (2000).

8. G. Thériault, Y. De Koninck, and N. McCarthy, "Extended depth of field microscopy for rapid volumetric two-photon imaging," Opt. Express **21**, 10095–10104 (2013).
9. G. Thériault, M. Cottet, A. Castonguay, N. McCarthy, and Y. De Koninck, "Extended two-photon microscopy in live samples with Bessel beams: steadier focus, faster volume scans, and simpler stereoscopic imaging," Front. Cell. Neurosci. **8**, 139 (2014).
10. H. Dehez, M. Piché, and Y. De Koninck, "Resolution and contrast enhancement in laser scanning microscopy using dark beam imaging," Opt. Express **21**, 15912–15925 (2013).
11. J. Arlt, V. Garcés-Chávez, W. Sibbett, and K. Dholakia, "Optical micromanipulation using a Bessel light beam," Opt. Commun. **197**, 239–245 (2001).
12. N. Olivier, D. Débarre, P. Mahou, and E. Beaurepaire, "Third-harmonic generation microscopy with Bessel beams: a numerical study," Opt. Express **20**, 24886–24902 (2012).
13. P. X. Liu, W. Shi, D. G. Xu, X. Z. Zhang, G. Z. Zhang, and J. Q. Yao, "Efficient phase-matching for difference frequency generation with pump of Bessel laser beams," Opt. Express **24**, 901–906 (2016).
14. N. Vuillemin, P. Mahou, D. Débarre, T. Gacoin, P.-L. Tharaux, S. K. Marie-Claire, W. Supatto, and E. Beaurepaire, "Efficient second-harmonic imaging of collagen in histological slides using Bessel beam excitation," Sci. Rep. **6**, 29863 (2016).
15. R. S. Bondurant, P. Kumar, J. H. Shapiro, and M. Maeda, "Degenerate four-wave mixing as a possible source of squeezed-state light," Phys. Rev. A **30**, 343–353 (1984).
16. J. Zheng and M. Katsuragawa, "Freely designable optical frequency conversion in Raman-resonant four-wave-mixing process," Sci. Rep. **5**, 8874 (2015).
17. X. M. Cheng, Z. Y. Ren, J. Wang, Y. Z. Miao, X. L. Xu, L. J. Jia, H. M. Fan, and J. T. Bai, "Quantitative measurement of rubidium isotope ratio using forward degenerate four-wave mixing," Spectrochim. Acta B **70**, 39–44 (2012).
18. X. L. Yin, X. M. Cheng, Y. Zhang, H. W. Chen, J. T. Bai, and Z. Y. Ren, "Measurement of lithium isotope ratio in various concentration samples using degenerate four-wave mixing," Appl. Opt. **54**, 7154–7159 (2015).
19. J. Feinberg, "Self-pumped, continuous-wave phase conjugator using internal reflection," Opt. Lett. **7**, 486–488 (1982).
20. K. R. Macdonald, W. R. Tompkin, and R. W. Boyd, "Passive one-way aberration correction using four-wave mixing," Opt. Lett. **13**, 485–487 (1988).
21. N. Chen, "Phase-conjugated distortion by degenerate four-wave mixing," Opt. Commun. **59**, 69–71 (1986).
22. S. Trillo and S. Wabnitz, "Nonlinear phase distortion in phase conjugation by degenerate four-wave mixing in Kerr media," J. Opt. Soc. Am. B **5**, 195–201 (1988).
23. Q. Zhang, X. M. Cheng, H. W. Chen, B. He, Z. Y. Ren, Y. Zhang, and J. T. Bai, "Diffraction-free, self-reconstructing Bessel beam generation using thermal nonlinear optical effect," Appl. Phys. Lett. **111**, 161103 (2017).
24. R. M. Herman and T. A. Wiggins, "Production and uses of diffractionless beams," J. Opt. Soc. Am. A **8**, 932–942 (1991).
25. N. Chattrapiban, E. A. Rogers, D. Cofield, W. T. Hill, 3rd, and R. Roy, "Generation of nondiffracting Bessel beams by use of a spatial light modulator," Opt. Lett. **28**, 2183–2185 (2003).
26. D. A. Steck, "Rubidium 85 D (87 D) line data," revision 2.1.2, August 12, 2009, http://steck.us/alkalidata.
27. S. K. Tiwari, S. R. Mishra, S. P. Ram, and H. S. Rawat, "Generation of a Bessel beam of variable spot size," Appl. Opt. **51**, 3718–3725 (2012).
28. Y. Zhang, X. M. Cheng, X. L. Yin, J. T. Bai, P. Zhao, and Z. Y. Ren, "Research of far-field diffraction intensity pattern in hot atomic Rb sample," Opt. Express **23**, 5468–5476 (2015).